



# Efficient inhibition of photogenerated electron-hole recombination through persulfate activation and dual-pathway degradation of micropollutants over iron molybdate

Liang Wang<sup>a,b</sup>, Xuan Huang<sup>a,b</sup>, Muen Han<sup>c</sup>, Lai Lyu<sup>c,\*</sup>, Tong Li<sup>c,d</sup>, Yaowen Gao<sup>c</sup>, Qingyi Zeng<sup>c</sup>, Chun Hu<sup>c,d</sup>

<sup>a</sup> State Key Laboratory of Separation Membranes and Membrane Processes, Tianjin Polytechnic University, Tianjin 300387, China

<sup>b</sup> School of Environmental and Chemical Engineering, Tianjin Polytechnic University, Tianjin 300387, China

<sup>c</sup> Key Laboratory for Water Quality and Conservation of the Pearl River Delta, Ministry of Education, Institute of Environmental Research at Greater Bay, Guangzhou University, Guangzhou 510006, China

<sup>d</sup> Key Laboratory of Drinking Water Science and Technology, Research Center for Eco-Environmental Sciences, Chinese Academy of Sciences, Beijing 100085, China

## ARTICLE INFO

### Keywords:

Iron molybdate

Photocatalysis

Electron-hole recombination

Persulfate activation

Micropollutant degradation

## ABSTRACT

Photogenerated electron-hole recombination has been a bottleneck problem for photocatalytic reactions for a long time. Herein, we propose an efficient solution strategy through capturing electrons and holes with environmental factors. In this study, nanoscale iron molybdate ( $\text{Fe}_2(\text{MoO}_4)_3$ ) was successfully synthesized, characterized and used in a heterogeneous photo-combined persulfate (PS) activation (HPPA) process for micropollutant removal. The reaction rate in this system was  $\sim 98$  and  $\sim 59$  times higher for Fenton-like and photocatalytic oxidation alone, respectively, which was attributed to strong synergistic effects of HPPA process. During the HPPA reaction, PS could quickly capture the photogenerated electrons to produce sulfate radicals ( $\text{SO}_4^{\cdot-}$ ), which was further converted to hydroxyl radicals ( $\cdot\text{OH}$ ) in water. Induced by PS, the electron-rich pollutants could actively capture the holes and be oxidized and degraded. This synergistic process not only inhibited the electron-hole recombination but also enabled rapid dual-pathway degradation of pollutants through free radical attack and hole oxidation.

## 1. Introduction

The release and spread of refractory micropollutants, such as pharmaceuticals, pesticides, hormones, personal care products and endocrine disrupting compounds, in water environments is regarded as a global environmental problem that cannot be ignored [1–3]. Conventional wastewater treatment technologies have proven to be ineffective in removing these micropollutants [4]. Therefore, it is necessary to develop more powerful and efficient technologies for this purpose.

Semiconductor photocatalysis, in which unlimited and eco-friendly solar energy can be acquired as a renewable resource, has been regarded as one of the most important prospective technologies for the degradation of micropollutants [5–12]. Production of electron-hole pairs under photoexcitation is the core step in solar energy conversion. Nevertheless, most of the photogenerated electron-hole pairs are wasted by recombination in the bulk, which is extremely unfavorable

for the efficiency and activity of the photocatalytic reaction. Therefore, various efforts have been devoted to promoting the performance of photocatalysis by boosting the separation efficiency of photogenerated electron-hole pairs, such as doping noble metal element Ag and Au [13–15], deposition of C and N species [16,17] and construction of heterogeneous structures with two different semiconductors [9,18–21]. Recently, we found that improving the ability to capture electrons and holes respectively by other participatory substances, such as pollutants, persulfate and  $\text{O}_2$ , is also conducive to enhancing the charge utilization efficiency and promoting the photocatalytic efficiency.

Hybrid advanced oxidation processes (HAOPs), which combine activation of hydrogen peroxide ( $\text{H}_2\text{O}_2$ ), persulfate (PS) or peroxymonosulfate (PMS) with other advanced oxidation technologies, such as light irradiation [12,22], microwave irradiation [23] and ultrasonic irradiation [24,25], are proven to have great potential for removing refractory organic pollutants due to the rapid generation of variously aggressive active species such as hydroxyl radicals ( $\cdot\text{OH}$ ), sulfate

\* Corresponding author.

E-mail address: [lyulai@gzhu.edu.cn](mailto:lyulai@gzhu.edu.cn) (L. Lyu).

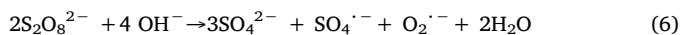
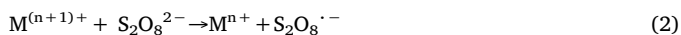
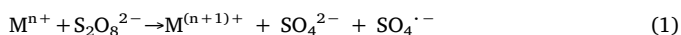
<https://doi.org/10.1016/j.apcatb.2019.117904>

Received 20 May 2019; Received in revised form 17 June 2019; Accepted 24 June 2019

Available online 28 June 2019

0926-3373/ © 2019 Elsevier B.V. All rights reserved.

radicals ( $\text{SO}_4^{\cdot-}$ ), superoxide radicals ( $\text{O}_2^{\cdot-}$ ) and singlet oxygen ( $^1\text{O}_2$ ). The heterogeneous photocombined PS/PMS activation (HPPA) process, consisting of visible light irradiation and activation of the PS/PMS by solid catalyst, is one of the most promising HAOPs and is widely studied. Among the developed HPPA processes, some catalysts, such as  $\text{Co-TiO}_2$  [26],  $\text{PI-g-C}_3\text{N}_4$  [27],  $\text{g-C}_3\text{N}_4\text{-INA-FePcCl}_{16}$  [28] and  $\text{g-C}_3\text{N}_4\text{-IMA-FePcCl}_{16}$  [29], exhibit dual functions for independent activation of PS/PMS and photocatalytic reaction, while some catalysts, such as magnetic spinel ferrites  $\text{CoFe}_2\text{O}_4$  and  $\text{CuFe}_2\text{O}_4$  [30,31], mainly promote PS/PMS activation with the assistance of light irradiation. Recent studies have found that the HPPA reaction is not a simple mathematical addition process for activity enhancement but a synergistic promotion process full of various possibilities [32]. Taking the photocombined activation of PS as an example, PS can not only be activated by the catalyst or light irradiation to generate free radicals ( $\text{SO}_4^{\cdot-}$ ,  $\text{S}_2\text{O}_8^{\cdot-}$ ,  $\cdot\text{OH}$  and  $\text{O}_2^{\cdot-}$  et al.) directly or indirectly through the redox cycle reaction (Eqs. (1)–(6)) [33–36] but also serve as acceptors of photo-generated electrons ( $e^-$ ) and holes ( $h^+$ ) to prevent their recombination, accompanied by the generation of more reactive radicals (Eqs. (7) and (8)). The photogenerated  $e^-$  can also regenerate the active transition metal (M) ions over the catalyst by the reduction of  $\text{M}^{(n+1)+}$  to  $\text{M}^{n+}$ , promoting the degradation efficiency of the contaminants.



The synergistic promotion effects of HPPA reactions show great promise for future applications in water purification. However, the specific reaction mechanism of the synergistic effects and the suppression pathway of the electron-hole recombination are still unclear due to the complexity of the radical chain reactions, which are a huge bottleneck for the application of this technology. In addition, the most common catalysts for PS/PMS activation are the cobalt series catalysts, due to the  $\text{Co}^{2+}$ /PMS system having the best effect for  $\text{SO}_4^{\cdot-}$  generation. However, the application of Co-containing catalysts is greatly limited because of the potential carcinogenic effects of the released Co species [28,37]. Therefore, it is of great significance to develop novel, environmentally friendly, efficient and stable HPPA catalysts and reveal their complex interfacial reaction mechanisms and the suppression pathways of the electron-hole recombination for the application of this technology.

In this work, a novel HPPA catalyst consisting of the emerging metal molybdate  $\text{Fe}_2(\text{MoO}_4)_3$  nanoparticles was successfully synthesized by a facile hydrothermal process and characterized by powder X-ray diffraction (XRD) analysis, X-ray photoelectron spectroscopy (XPS), UV–vis diffuse reflectance spectroscopy (UV–vis DRS), Fourier transform infrared spectroscopy (FTIR) and Raman spectroscopy.  $\text{Fe}_2(\text{MoO}_4)_3$  exhibited exceptionally high activity for PS activation and refractory pollutant degradation under visible light irradiation, accompanied by the generation of active free radicals. The photoelectrochemical performance of the  $\text{Fe}_2(\text{MoO}_4)_3$  HPPA process was also significantly enhanced by the synergistic effects. It was found that PS could quickly capture the photogenerated electrons to produce  $\text{SO}_4^{\cdot-}$ , which were immediately converted into  $\cdot\text{OH}$  radicals in water. Induced by PS, the electron-rich pollutants actively captured the holes and were oxidized and degraded. This synergistic process not only inhibited the

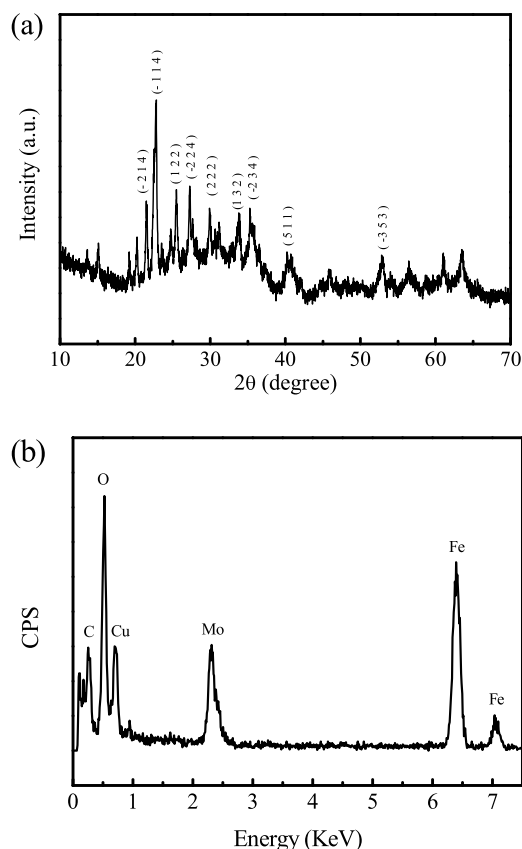


Fig. 1. (a) XRD pattern of  $\text{Fe}_2(\text{MoO}_4)_3$ . (b) EDS pattern of  $\text{Fe}_2(\text{MoO}_4)_3$ .

electron-hole recombination but also enabled rapid degradation of pollutants through free radical attack and hole oxidation. The interfacial reaction processes and electron-hole recombination inhibition mechanisms have been revealed through spin trapping-electron paramagnetic resonance (EPR) analysis.

## 2. Materials and methods

### 2.1. Chemicals and reagents

Sodium molybdate dehydrate ( $\text{Na}_2\text{MoO}_4 \cdot 2\text{H}_2\text{O}$ ), sodium sulfate ( $\text{Na}_2\text{SO}_4$ ), Acid Orange 7 (AO7), and 2,4-Dichlorophenoxyacetic acid (2,4-D) were purchased from Shanghai Titan Scientific Co., Ltd. Bisphenol A (BPA), phenytoin (PHT), ciprofloxacin (CIP), methylene blue (MB), and methyl orange (MO) were obtained from Sinopharm Chemical Reagent Co., Ltd. Ferrous acetate ( $\text{Fe}(\text{CH}_3\text{COO})_2$ ) was provided by Tokyo Chemical Industry Co., Ltd. Sodium persulfate ( $\text{Na}_2\text{S}_2\text{O}_8$ ) was from Shanghai Tanchem Co., Ltd. Rhodamine B (RhB) was provided by Beijing Xinjingke Biotechnologies Co., Ltd. 5-tert-butoxycarbonyl-5-methyl-1-pyrroline-N-oxide (BMPO) was supplied by the Bioanalytical Lab (Sarasota, FL). All chemicals were at least analytical grade, and ultrapure water was used throughout this research.

### 2.2. Catalyst preparation

$\text{Fe}_2(\text{MoO}_4)_3$  was synthesized by a facile hydrothermal method. Typically, 5 mmol sodium molybdate dehydrate and 5 mmol ferrous acetate were successively added to 150 mL ultrapure water. The abovementioned solution was magnetically stirred at 25 °C for 10 min. After ultrasonic processing in a water bath for 10 min, the mixture was stirred for another 10 min to spread the solute. Then the solution was transferred to a 200 mL Teflon-coated steel autoclave and heated at 140 °C for 12 h to obtain the liquid precursor. After cooling naturally to

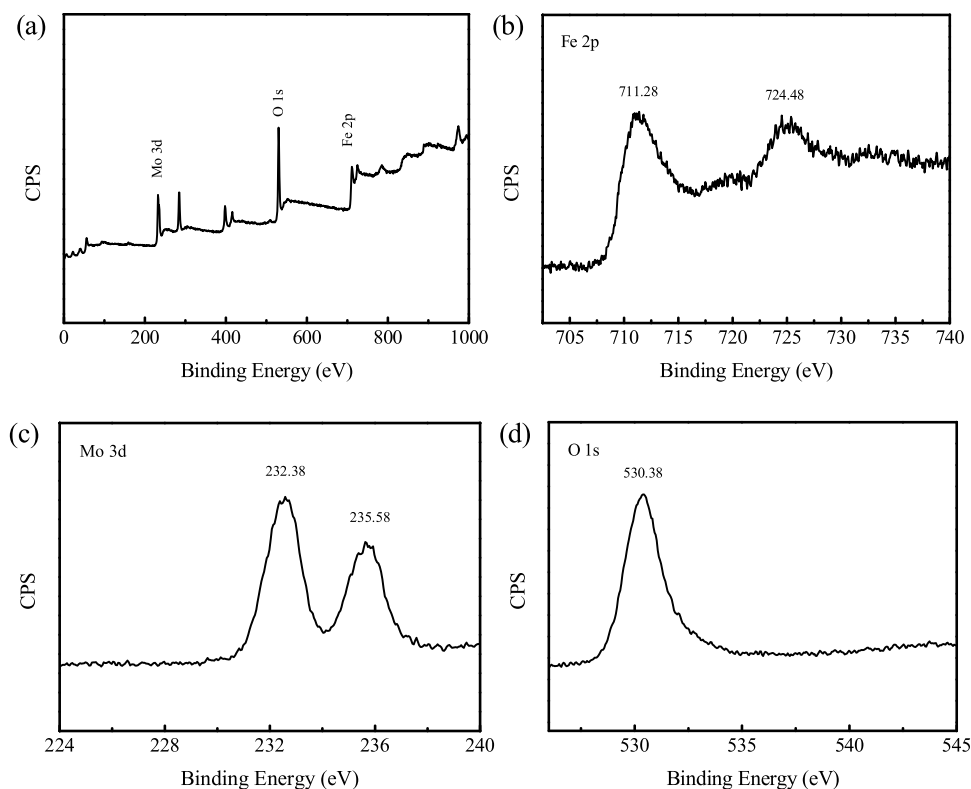


Fig. 2. XPS spectra of the prepared  $\text{Fe}_2(\text{MoO}_4)_3$ : (a) survey, (b) Fe 2p, (c) Mo 3d and (d) O 1s.

room temperature, the precursor solution was filtered and washed with ultrapure water several times and dried at  $60^\circ\text{C}$  for 6 h. After it was ground to a powder and collected in an alumina crucible without a cover, the obtained product was heated up to  $500^\circ\text{C}$  with a ramp rate of  $2^\circ\text{C min}^{-1}$  and kept for 4 h.

### 2.3. Catalyst characterization and electrochemical measurements

The microstructure of the sample was observed with a JEOL-2100 transmission electron microscopy (TEM), and high-resolution transmission electron microscopy (HRTEM) images were also obtained with an acceleration voltage of 200 kV. The phase structure of the  $\text{Fe}_2(\text{MoO}_4)_3$  was evaluated by powder X ray diffraction (XRD) patterns on a Scintag-XDS-2000 diffractometer using Cu K $\alpha$  radiation ( $\lambda = 1.540598 \text{ \AA}$ ) operating at 40 kV and 40 mA, with a scanning rate of  $8^\circ \text{ min}^{-1}$ . The X-ray photoelectron spectroscopy (XPS) data were obtained using an AXIS-Ultra instrument from Kratos using monochromatic Al K $\alpha$  radiation (225 W, 15 mA, 15 kV) and low-energy electron flooding for charge compensation. FTIR spectra were obtained via a Nicolet 8700 FTIR spectrophotometer (Thermo Fisher Scientific Inc., USA) in the range of  $4000\text{--}400 \text{ cm}^{-1}$ . The dry catalyst powder was supported on KBr pellets at a fixed proportion (1 wt%). The Raman spectra were measured via a LabRAM HR Evolution (HORIBA, France) with a 532-nm excitation laser. The electron paramagnetic resonance (EPR) spectra were obtained using a Bruker A300-10/12 ESR spectrometer (center field: 3480.00 G; microwave frequency: 9.86 GHz; and microwave power: 2.29 mW) at room temperature. The UV–vis diffuse reflectance spectroscopy (UV–vis DRS) data and UV–vis spectra were collected with a Hitachi U-3900 spectrophotometer.

Electrochemical measurements were carried out in a standard three-electrode quartz cell system (the as-synthesized samples, Pt foil and Ag/AgCl electrode as working, counter and reference electrodes, respectively) with a 0.1 M  $\text{Na}_2\text{SO}_4$  electrolyte solution and an electrochemical system (CHI 660D electrochemical workstation) under a 100 W xenon lamp with a 420-nm cutoff filter. Twenty mg catalyst was added to 1 mL

Nafion solution (0.5 wt%) by 30 min water bath sonication and 30 min vortexing to ensure dispersible uniformity. Then, 200  $\mu\text{L}$  of the suspension was collected and daubed onto the conductive surface of ITO conductive glass, which was dried naturally in air to form the working electrode.

### 2.4. Procedures and analysis methods

RhB, AO7, MO, MB, PHT, BPA, 2,4-D and CIP were chosen as representative refractory organic pollutants to estimate the performances of the catalysts. In a typical HPPA reaction, 0.05 g  $\text{Fe}_2(\text{MoO}_4)_3$  was added to the above pollutants solution (10 mg/L). Ahead of irradiation, the mixed solution was magnetically stirred for 30 min in the dark to reach the adsorption-desorption equilibrium. Then, persulfate (4 mM) was added to the suspension, and the 300-W xenon lamp (Perfect Light, China) with a UV cutoff filter ( $\lambda > 420 \text{ nm}$ ) was turned on to provide light source. At given time intervals, 2 mL aliquots were taken out and filtered through a Millipore filter (pore size  $0.45 \mu\text{m}$ ) to remove the catalyst, and then excessive  $\text{NaNO}_2$  was added to prevent the further reaction of remnant persulfate.

The concentrations of BPA and PHT were analyzed with a 1200 series HPLC (Agilent, U.S.A.) that was equipped with a UV detector and a Zorbax SB-Aq column ( $5 \mu\text{m}$ ,  $4.6 \times 250 \text{ mm}$ ; Agilent). For BPA, the mobile phase was a mixture of 70% methanol and 30% water with a flow rate of  $1.0 \text{ mL min}^{-1}$ , and the UV detector was operated at 225 nm. For PHT, the mobile phase was a mixture of acetonitrile and water containing 0.08% phosphoric acid (60:40, v/v) with a flow rate of  $1.0 \text{ mL min}^{-1}$ , and the UV detector was operated at 220 nm.

To measure the concentration of organic dye after the reaction, a UV–vis spectrophotometer (UV-3900, Shimadzu) was used. The maximum absorption wavelengths for RhB, AO7, MO and MB were 554 nm, 485 nm, 464 nm, and 669 nm respectively. The total organic carbon (TOC) was measured with a Shimadzu TOC-V $_{\text{C}_\text{PH}}$  analyzer. The basic principle of the TOC analyzer is high-temperature combustion. To test the recyclability and stability of the catalyst, the used  $\text{Fe}_2(\text{MoO}_4)_3$  was

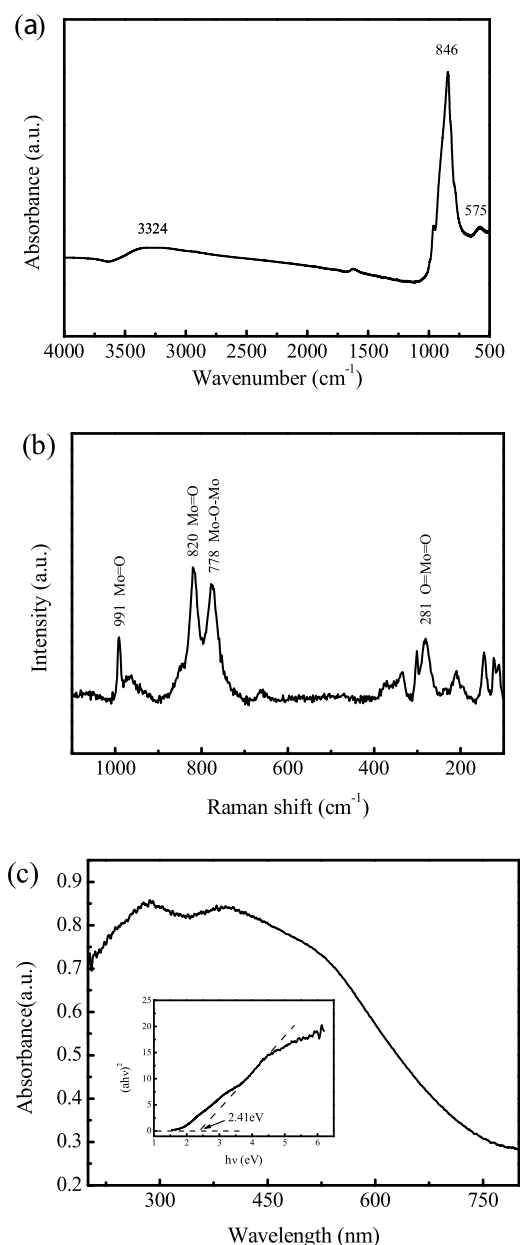


**Fig. 3.** (a) FTIR spectrum of the prepared  $\text{Fe}_2(\text{MoO}_4)_3$ . (b) Raman spectrum of the prepared  $\text{Fe}_2(\text{MoO}_4)_3$ . (c) UV-vis DRS and plots of  $(\alpha h\nu)^2$  versus photon energy ( $h\nu$ ) for the band gap energies of as-synthesized  $\text{Fe}_2(\text{MoO}_4)_3$  (inset).

collected by membrane filtration. After each reaction, the solid was washed with ultrapure water three times under neutral conditions. Then, the solid sample was dried at 60 °C for 6 h and reused in the next run.

BMPO-trapped EPR signals were detected in methanol or aqueous dispersions of the as-prepared sample, and the spectra were recorded with a Bruker A300-10/12 EPR spectrometer at room temperature. Specifically, in the absence of PS, 0.005 g of the powder sample and 4 mM PS were added to 1 mL of water (for detecting  $\cdot\text{OH}$ ) or methane (for detecting  $\text{O}_2^{\cdot-}$ ) in the dark for 2 min; then 100  $\mu\text{L}$  of suspension was transferred to 10  $\mu\text{L}$  of BMPO (200 mM) in the dark environment for another 2 min. Afterwards, the mixed solution was piled into the capillary. During the reaction of the HPPA system, both PS and light should participated. In this work, a 350-W xenon lamp (Perfect Light, China) with a UV cutoff filter ( $\lambda > 420 \text{ nm}$ ) was used to provide the light source. Typically, the same operation (with the absence of only

PS) went on until BMPO was added to the solution. Then, 10  $\mu\text{L}$  of BMPO (200 mM) was added to 100  $\mu\text{L}$  water/methanol suspension, which contained well-dispersed  $\text{Fe}_2(\text{MoO}_4)_3$  and PS. The xenon lamp was turned on for 2 min, and the solution was sucked into the capillary. To detect the EPR signal in the presence of pollutants in different reaction systems, 10 ppm BPA dissolved in water or methanol was prepared. The EPR signal was obtained by replacing the pure water or methanol solution with the as-prepared BPA water or methanol solution (10 mg/L) without changing any other experimental conditions.

### 3. Results and discussion

#### 3.1. Characterization of catalyst

The TEM images of the  $\text{Fe}_2(\text{MoO}_4)_3$  samples (Figure S1a, b, Supporting Information (SI)) revealed that they were predominantly in the shape of regular nanoparticles with a size range of 5–20 nm. Very obvious and neat lattice fringes with interplanar spacing of 0.324 nm and 0.387 nm, which correspond to the (-224) and (-114) crystal plane of  $\text{Fe}_2(\text{MoO}_4)_3$ , respectively (JCPDS file card No.35-0183), were observed in the HRTEM images of  $\text{Fe}_2(\text{MoO}_4)_3$  (Figure S1c, d), confirming the formation of a single crystalline structure by the prepared sample. The elemental mappings from TEM (Figure S1e) revealed that the main elements of the sample were Fe, O and Mo, which were highly dispersed into the framework of  $\text{Fe}_2(\text{MoO}_4)_3$ . Fig. 1a shows the powder XRD patterns of the prepared  $\text{Fe}_2(\text{MoO}_4)_3$ . The reflection peaks could be well-indexed to the orthorhombic phase (JCPDS file card No.35-0183) of  $\text{Fe}_2(\text{MoO}_4)_3$  with calculated lattice constants of  $a = 15.737 \text{ \AA}$ ,  $b = 9.231 \text{ \AA}$  and  $c = 18.224 \text{ \AA}$ . Several evident characteristic peaks were observed at  $21.56^\circ$ ,  $22.82^\circ$ ,  $25.5^\circ$ ,  $27.26^\circ$ ,  $29.92^\circ$ ,  $33.8^\circ$ ,  $35.28^\circ$ ,  $40.22^\circ$  and  $52.88^\circ$ , which correspond to (-2 1 4), (-1 1 4), (1 2 2), (-2 2 4), (2 2 2), (1 3 2), (-2 3 4), (5 1 1) and (-3 5 3) crystal planes, respectively. There were no evidently peaks indexed to  $\text{MoO}_3$  or  $\text{Fe}_2\text{O}_3$ , demonstrating that the catalyst consisted of a single phase. The energy dispersion X-ray (EDS) pattern of the as-prepared product in Fig. 1b confirmed that the elements in the sample were mainly Fe, Mo and O. The C peak in the spectrum could be attributed to  $\text{CO}_2$  adsorbed by the sample, and the Cu is from the substrate.

Surface elemental composition of the  $\text{Fe}_2(\text{MoO}_4)_3$  sample was analyzed by the XPS technique. As shown in Fig. 2a, Mo, O, and Fe elements could be identified from the full-spectrum. Fig. 2b shows two binding energy peaks surveyed at the energy positions of 711.28 and 724.48 eV, which substantiated the existence of Fe  $2p_{3/2}$  and Fe  $2p_{1/2}$ , respectively and were characteristic of  $\text{Fe}^{3+}$  in  $\text{Fe}_2(\text{MoO}_4)_3$  [38,39]. The Mo 3d spectrum (Fig. 2c) shows two distinct peaks at 232.38 and 235.58 eV, which authenticated the electronic state of molybdenum is  $\text{Mo}^{6+}$  [40,41]. Moreover, The O 1s peak (Fig. 2d) located at 530.38 eV corresponded to lattice oxygen in the  $\text{Fe}_2(\text{MoO}_4)_3$  phase, which could be attributed to the Fe–O bonds [42].

The FTIR spectroscopy of  $\text{Fe}_2(\text{MoO}_4)_3$  are shown in Fig. 3a. The characteristic band observed at  $3324 \text{ cm}^{-1}$  can be assigned to the stretching of O–H bonds of the surface hydroxyl groups present on the surface of the nanoparticles. The strong peak at  $846 \text{ cm}^{-1}$  and the weak peak at  $575 \text{ cm}^{-1}$  represented the vibration of Mo–Fe and Fe–O, respectively [43,44]. The bonding structure of the  $\text{Fe}_2(\text{MoO}_4)_3$  crystal can be further revealed by Raman spectra. As shown in Fig. 3b, the main features of the iron molybdate catalyst were the bands at 991, 820, 778 and  $281 \text{ cm}^{-1}$  ascribable to the symmetric stretching vibrations of Mo=O, antisymmetric stretching vibrations of Mo=O, stretching vibrations of Mo–O–Mo and wagging mode of lattice O=Mo=O bonds [44–46], respectively, indicating the stable bonding structure between Mo, Fe and O species.

The optical adsorption properties of the obtained powder are shown in Fig. 3c. It was found that the sample exhibited intense absorption bands in both UV and visible-light regions. The optical band gap ( $E_g$ ) of the obtained  $\text{Fe}_2(\text{MoO}_4)_3$  was calculated from the following equation

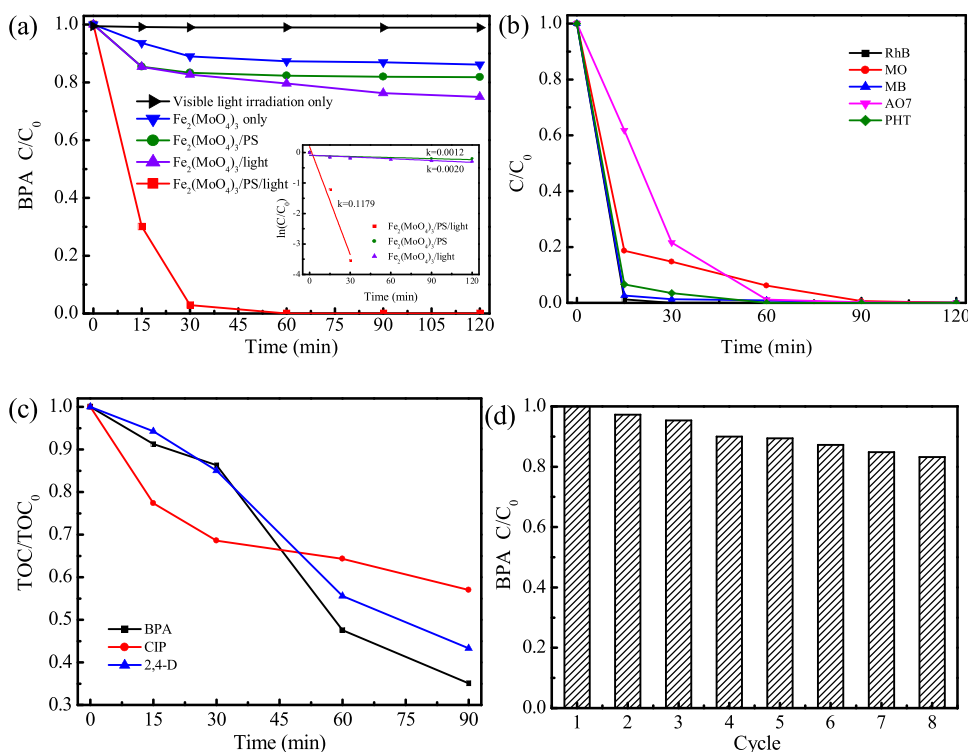


**Fig. 4.** (a) BPA degradation curves in various suspensions (Insert shows the corresponding kinetic curves). (b) Decomposition curves of different pollutants in Fe<sub>2</sub>(MoO<sub>4</sub>)<sub>3</sub> HPPA systems. (c) TOC removal curves during BPA degradation. (d) The reusability of Fe<sub>2</sub>(MoO<sub>4</sub>)<sub>3</sub> for BPA degradation in HPPA system. Reaction conditions: natural initial pH, initial pollutants concentration 10 mg L<sup>-1</sup>, initial PS concentration 4.0 mM, and catalyst concentration 1.0 g L<sup>-1</sup>.

(Eqs. (9)) [47]:

$$\alpha h\nu = A(h\nu - E_g)^{n/2} \quad (9)$$

On the left side of the equation,  $\alpha$ ,  $h$  and  $\nu$  represent absorption coefficient, Plank constant, and light frequency, respectively. On the other side of the equation,  $A$ ,  $E_g$  and  $n$  are a proportionality constant, optical band gap and the optical transition type of the semiconductor photocatalysis ( $n = 1$  for a direct transition), respectively. It was seen that the band gap energy of Fe<sub>2</sub>(MoO<sub>4</sub>)<sub>3</sub> was determined to be 2.41 eV (inset image of Fig. 3c), implying that light with a wavelength lower than 515 nm could be absorbed by the photocatalyst, giving direct band-to-band (valence band to conduction band) transition. Additionally, Fe<sub>2</sub>(MoO<sub>4</sub>)<sub>3</sub> could absorb light with wavelengths from 500 to 800 nm, which was ascribed to a Mo<sup>5+</sup> d-d transition or the Mo<sup>5+</sup>-Mo<sup>6+</sup> charge transfer. [41,48]

### 3.2. Catalytic performance evaluation for pollutant degradation

The catalytic activity of Fe<sub>2</sub>(MoO<sub>4</sub>)<sub>3</sub> in the HPPA process was assessed for degradation of the endocrine disruptor pollutant BPA, which can be naturally degraded in over 90 years [49]. As illustrated in Fig. 4a, there was almost no degradation of BPA under visible light irradiation alone, and a weak removal effect (~13%) for BPA was observed in a solitary catalyst system within 120 min. The degradation rate of BPA increased to 18.2% and 25.0% in 120 min in the Fe<sub>2</sub>(MoO<sub>4</sub>)<sub>3</sub>/PS and Fe<sub>2</sub>(MoO<sub>4</sub>)<sub>3</sub>/light systems, respectively, suggesting weak photocatalytic and PS activation performances of Fe<sub>2</sub>(MoO<sub>4</sub>)<sub>3</sub>. However, the BPA degradation rate dramatically increased to 97.1% in just 30 min and reached 100% in 60 min in the Fe<sub>2</sub>(MoO<sub>4</sub>)<sub>3</sub>/PS/light HPPA system, which was ~98 and ~59 times faster than that in the Fe<sub>2</sub>(MoO<sub>4</sub>)<sub>3</sub>/PS and Fe<sub>2</sub>(MoO<sub>4</sub>)<sub>3</sub>/light systems, respectively (Fig. 4a insert). A strong synergistic effect between photocatalysis and PS activation was reflected in the HPPA system for pollutant degradation. To further investigate the activity and adaptability of the HPPA system, synthetic dyes RhB, MO, MB, and AO7 and pharmaceutical pollutant PHT were degraded in the Fe<sub>2</sub>(MoO<sub>4</sub>)<sub>3</sub>/PS/light HPPA system. Before the reaction, the adsorption rates for these pollutants were 11%–40%,

which was conducive to the efficient and rapid degradation of pollutants on the catalyst surface. As illustrated in Fig. 4b, all contaminants could be completely removed within 120 min, especially RhB, MB and PHT, which were almost completely degraded in 15 min. In addition, TOC removal reached 43–65% (reaction 90 min) during the degradation of endocrine disruptor BPA, pharmaceutical CIP and pesticide 2,4-D in the HPPA system (Fig. 4c). These results suggested that the HPPA system possessed excellent catalytic performance and adaptability to various pollutants. We also assessed the durability of Fe<sub>2</sub>(MoO<sub>4</sub>)<sub>3</sub> by means of repeated and continuous activity evaluations after recovering the solid catalyst through washing and drying. As illustrated in Fig. 4d, the activity of the catalyst slightly decreased with the cyclic reaction, but the degradation rate for BPA still reached ~85% after seven consecutive reactions and remained stable in the following cycle, indicating the stability and durability of the catalyst. Such inferences were also supported by the XPS spectrum (Figure S2), for which the peak patterns and positions were almost unchanged after reaction in HPPA system. Compared with the pure catalyst, the FTIR peaks at 846 cm<sup>-1</sup> and 575 cm<sup>-1</sup> were also unchanged after reactions (Figure S3), confirming the stability of Fe<sub>2</sub>(MoO<sub>4</sub>)<sub>3</sub>. However, the peak for O–H bonds at 3324 cm<sup>-1</sup> apparently shifted to lower frequencies as the reaction continued, indicating the complexing adsorption between the pollutant and the metal sites on catalyst surface.

### 3.3. Enhanced photoelectrochemical performance of HPPA synergistic process

Representative current density versus voltage (I–V) characteristics of Fe<sub>2</sub>(MoO<sub>4</sub>)<sub>3</sub> under different conditions are presented in Fig. 5a. In the Fe<sub>2</sub>(MoO<sub>4</sub>)<sub>3</sub>/light and Fe<sub>2</sub>(MoO<sub>4</sub>)<sub>3</sub>/light/BPA systems, the photocurrent densities were relatively low. However, in the Fe<sub>2</sub>(MoO<sub>4</sub>)<sub>3</sub>/light/PS and Fe<sub>2</sub>(MoO<sub>4</sub>)<sub>3</sub>/light/PS/BPA systems, a large increase in the photocurrent densities were observed across the potential window, indicating the strong synergistic promotion effect of PS for the photocatalytic process. In addition, the pollutants played a positive role in this synergistic process. The Chronoamperometric technique was applied for reflecting the current-response of Fe<sub>2</sub>(MoO<sub>4</sub>)<sub>3</sub> under different conditions via



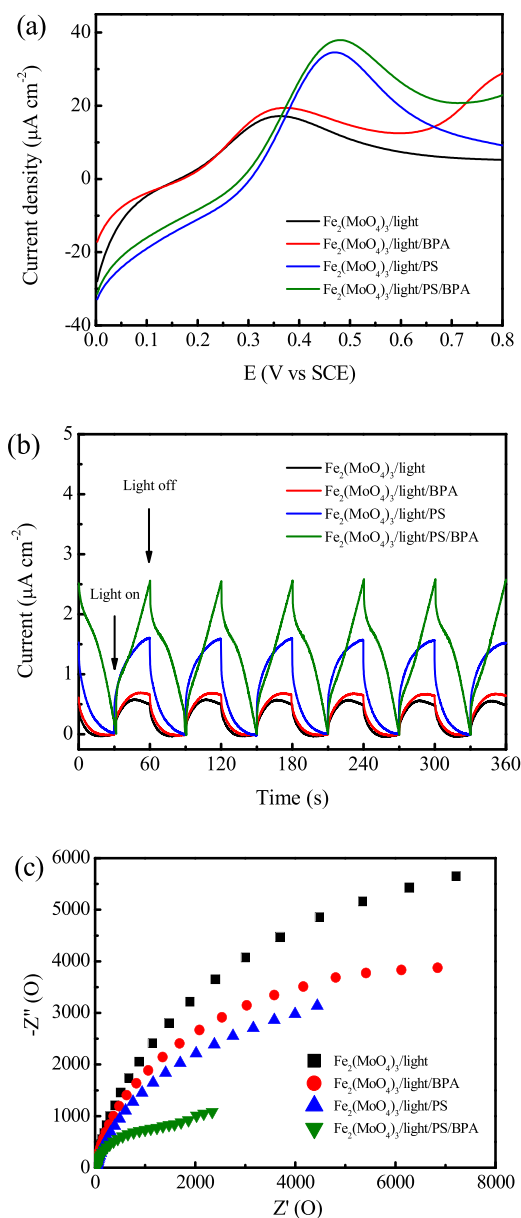


**Fig. 5.** (a) Representative current density versus voltage (I-V) characteristics of  $\text{Fe}_2(\text{MoO}_4)_3$  under different conditions. (b) Instantaneous photocurrent of  $\text{Fe}_2(\text{MoO}_4)_3$  under different conditions. (c) The electrochemical impedance spectroscopy (EIS) Nyquist plots of  $\text{Fe}_2(\text{MoO}_4)_3$  under different conditions.

several on-off cycles of irradiation. As illustrated in Fig. 5b, upon photoexcitation, the pure  $\text{Fe}_2(\text{MoO}_4)_3$  exhibited instantaneous photocurrent ( $\sim 0.5 \mu\text{A cm}^{-2}$ ), which then sharply reverted to steady state after turning off the light. After adding BPA to the  $\text{Fe}_2(\text{MoO}_4)_3$  electrode system, no current changes were observed, indicating that the individual contaminants were insufficient to affect the current density of the system. However, after adding PS to the  $\text{Fe}_2(\text{MoO}_4)_3$  electrode system, the photocurrent density instantaneously increased to three times that of the original  $\text{Fe}_2(\text{MoO}_4)_3$  electrode system under the visible light irradiation, indicating that the  $\text{Fe}_2(\text{MoO}_4)_3$  electrode had a better visible light response and more charge transfer with the assistance of PS. When PS and BPA coexisted in the electrolyte solution, the photocurrent density was further enhanced, five times that of the original  $\text{Fe}_2(\text{MoO}_4)_3$  electrode system under the visible light irradiation, thus confirming the positive role of the pollutants in this HPPA synergistic

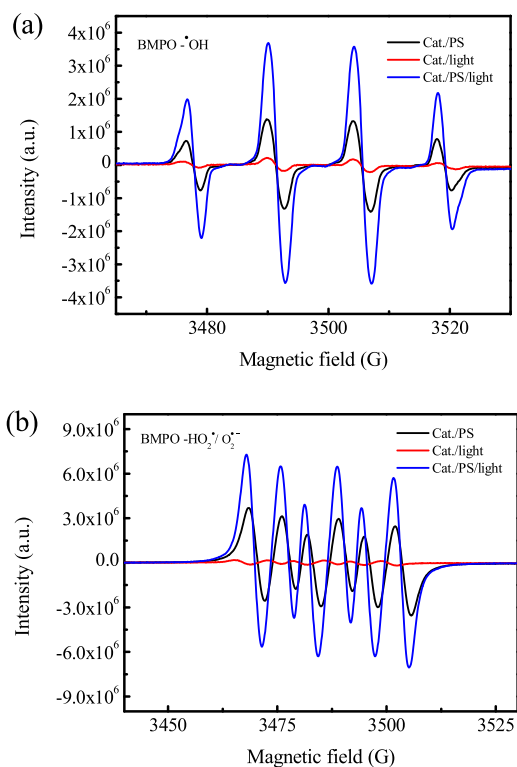


**Fig. 6.** BMPO spin-trapping EPR spectra for (a)  $\cdot\text{OH}$  and (b)  $\text{HO}_2\cdot/\text{O}_2\cdot^-$  in  $\text{Fe}_2(\text{MoO}_4)_3$  suspensions under different conditions: catalyst/PS, catalyst/light and catalyst/PS/light.

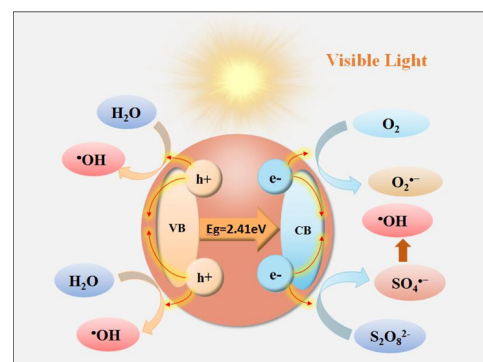


**Fig. 7.** Schematic illustration for the synergistic reaction mechanism in the  $\text{Fe}_2(\text{MoO}_4)_3$  HPPA process without pollutants.

process. The gradual increase/attenuation of the photocurrent density spikes were caused by the trapping of electrons and holes by PS and pollutants, respectively.

The electrochemical impedance spectroscopy (EIS) Nyquist plots were carried out to reflect the interfacial charge transfer rate in the HPPA processes. A smaller arc radius of the EIS Nyquist plot represents a faster electron transfer rate and a more efficient electron-hole separation. As shown in Fig. 5c, the arc radius on the EIS Nyquist plot followed the order of  $\text{Fe}_2(\text{MoO}_4)_3/\text{light/PS/BPA}$  system  $<<$   $\text{Fe}_2(\text{MoO}_4)_3/\text{light/PS}$  system  $<$   $\text{Fe}_2(\text{MoO}_4)_3/\text{light/pollutants}$  system  $<$   $\text{Fe}_2(\text{MoO}_4)_3/\text{light}$  system, suggesting that the synergistic processes of visible light irradiation and activation of PS led to more effective separation of photogenerated electron-hole pairs and faster interfacial charge transfer. With the coexistence of pollutants and PS, the interfacial electron transfer rate and the electron-hole separation efficiency of the HPPA system greatly improved.

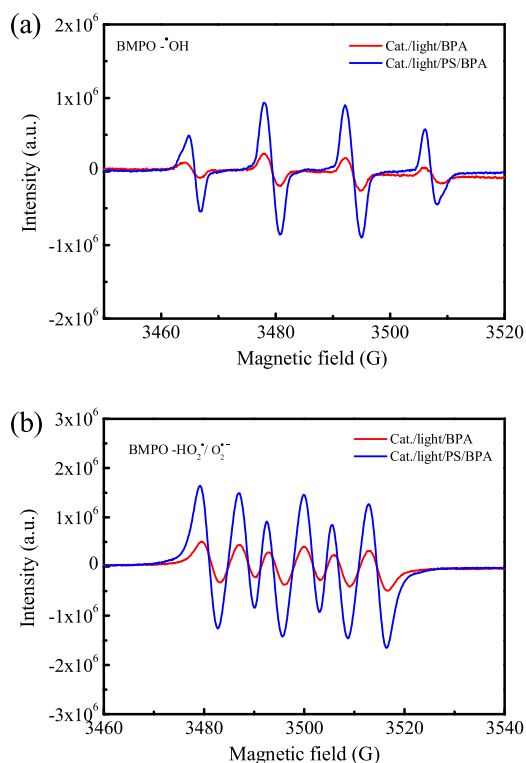


**Fig. 8.** BMPO spin-trapping EPR spectra for (a)  $\cdot\text{OH}$  and (b)  $\text{HO}_2\cdot/\text{O}_2^{\cdot-}$  in  $\text{Fe}_2(\text{MoO}_4)_3$  suspensions after adding BPA under visible light irradiation with/without PS.

### 3.4. Interfacial reaction process and electron-hole recombination inhibition mechanism

Electron paramagnetic resonance (EPR) analysis followed by radical trapping with 5-tert-butoxycarbonyl-5-methyl-1-pyrroline-N-oxide (BMPO) was carried out to gain deeper insights into the reactions. In the  $\text{Fe}_2(\text{MoO}_4)_3/\text{PS}$  system, no obvious signals for  $\text{BMPO}\text{-SO}_4^{\cdot-}$  were observed, but four moderate-intensity  $\text{BMPO}\text{-}\cdot\text{OH}$  signals with equal spacing and an intensity ratio of 1:2:2:1 (Fig. 6a) and six successive  $\text{BMPO}\text{-HO}_2\cdot/\text{O}_2^{\cdot-}$  signals (Fig. 6b) were observed, indicating that PS and the dissolved oxygen ( $\text{DO}$ ) species could be activated to radicals by  $\text{Fe}_2(\text{MoO}_4)_3$  to a certain degree. In the  $\text{Fe}_2(\text{MoO}_4)_3/\text{light}$  system, four  $\text{BMPO}\text{-}\cdot\text{OH}$  signals (Fig. 6a) and six  $\text{BMPO}\text{-HO}_2\cdot/\text{O}_2^{\cdot-}$  signals (Fig. 6b) were still observed, suggesting the photoactivation properties of  $\text{Fe}_2(\text{MoO}_4)_3$  resulted in the oxidation of  $\text{H}_2\text{O}$  to  $\cdot\text{OH}$  by holes and the reduction of  $\text{DO}$  to  $\text{O}_2^{\cdot-}$  by the photogenerated electrons. However, both signal intensities of  $\cdot\text{OH}$  and  $\text{O}_2^{\cdot-}$  were very weak, indicating a

strong electron-hole recombination effect in this system. After combining the visible light irradiation and PS activation process, the strongest  $\text{BMPO}\text{-}\cdot\text{OH}$  (Fig. 6a) and  $\text{BMPO}\text{-HO}_2\cdot/\text{O}_2^{\cdot-}$  signals (Fig. 6b) appeared in the  $\text{Fe}_2(\text{MoO}_4)_3/\text{PS}/\text{light}$  HPPA system. This result indicated that the synergistic effect of PS and light irradiation promoted the efficiency of electron-hole separation. As shown in (Fig. 7), on the one hand,  $\text{H}_2\text{O}$  captured more holes in the valence band and generated  $\cdot\text{OH}$  radicals, while  $\text{DO}$  obtained more electrons in the conduction band to produce copious  $\text{O}_2^{\cdot-}$  radicals; on the other hand, PS also obtained more electrons in the conduction band and was rapidly activated into free radicals.  $\text{SO}_4^{\cdot-}$  radicals were not apparently observed, because they were rapidly converted to  $\cdot\text{OH}$  radicals in the water environment. In this HPPA system, water acted as the original electron donor, while PS acted as the ultimate electron acceptor.

To investigate the interfacial interactions between pollutants/PS and  $\text{Fe}_2(\text{MoO}_4)_3$  under light irradiation, as well as the effects of pollutants and PS on electron-hole recombination, EPR analysis of the  $\text{Fe}_2(\text{MoO}_4)_3$  HPPA process in the presence of BPA followed by radical trapping with BMPO was carried out. In the  $\text{Fe}_2(\text{MoO}_4)_3/\text{light}/\text{BPA}$  system, four weak  $\text{BMPO}\text{-}\cdot\text{OH}$  signals (Fig. 8a) and six  $\text{BMPO}\text{-HO}_2\cdot/\text{O}_2^{\cdot-}$  signals (Fig. 8b) were detected, and their intensities were similar to those in the  $\text{Fe}_2(\text{MoO}_4)_3/\text{light}$  system, indicating that the production of the free radicals were not influenced by the pollutants in the solitary photocatalytic system. This result implied that the pollutants did not capture the holes directly to change the photocatalytic reaction pathway by suppressing electron-hole recombination in the  $\text{Fe}_2(\text{MoO}_4)_3/\text{light}/\text{BPA}$  system (Fig. 9a). Therefore, the degradation rate of pollutants under visible light irradiation alone was very slow in the activity evaluation experiments. After adding PS to the above system, the signal intensities of  $\text{BMPO}\text{-}\cdot\text{OH}$  were greatly enhanced in the  $\text{Fe}_2(\text{MoO}_4)_3/\text{light}/\text{PS}/\text{BPA}$  system (Fig. 8a) and were approximately four times higher than the signal intensities of the system without PS. Additionally, the pollutants were greatly degraded in the  $\text{Fe}_2(\text{MoO}_4)_3/\text{light}/\text{PS}/\text{pollutants}$  system according to the activity evaluations above. In addition, compared with the relative intensity of  $\text{BMPO}\text{-HO}_2\cdot/\text{O}_2^{\cdot-}$  ( $7.3 \times 10^6$ ) in the  $\text{Fe}_2(\text{MoO}_4)_3/\text{PS}/\text{light}$  system (Fig. 6b), the  $\text{BMPO}\text{-HO}_2\cdot/\text{O}_2^{\cdot-}$  intensity ( $1.6 \times 10^6$ ) in the  $\text{Fe}_2(\text{MoO}_4)_3/\text{light}/\text{PS}/\text{BPA}$  system was sharply decreased (Fig. 8b), indicating that the addition of pollutants captured holes and allowed more electrons to be effectively utilized by PS without being captured by  $\text{O}_2$  to generate  $\text{O}_2^{\cdot-}$  radicals. These results revealed a synergistic process of PS and pollutants for promoting the electron-hole separation under light irradiation in the  $\text{Fe}_2(\text{MoO}_4)_3/\text{light}/\text{PS}/\text{pollutants}$  HPPA system. As shown in Fig. 9b, pollutants and PS could be adsorbed on the surface of the catalyst under dark conditions, and photogenerated electrons and holes were produced with the visible light irradiation. As an electrophilic species, PS could quickly capture the photogenerated electrons to produce  $\text{SO}_4^{\cdot-}$ , which were immediately converted to  $\cdot\text{OH}$  radicals in water. Induced

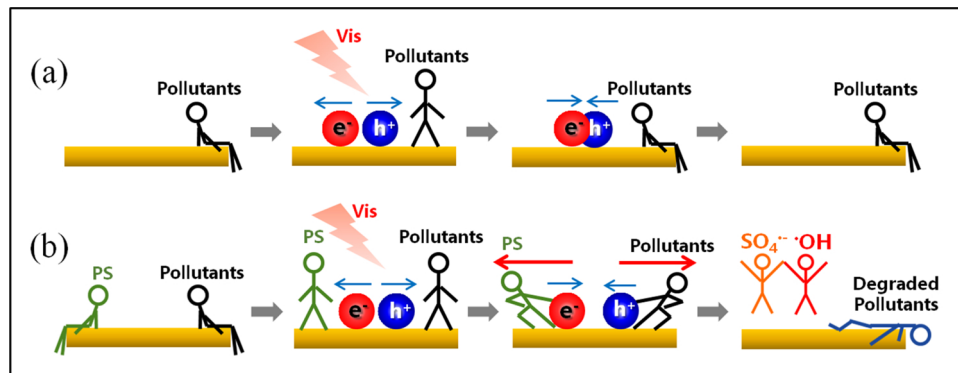


**Fig. 9.** Schematic illustration for the synergistic process of PS and pollutants for promoting the electron-hole separation under light irradiation in the  $\text{Fe}_2(\text{MoO}_4)_3/\text{light}/\text{PS}/\text{pollutants}$  HPPA system.

by PS, the electron-rich pollutants will actively capture the holes and be oxidized and degraded. This synergistic process not only inhibited the electron-hole recombination but also enabled rapid degradation of pollutants through free radical attack and hole oxidation.

#### 4. Conclusions

In response to photogenerated electron-hole recombination during photocatalytic processes, we demonstrated an efficient HPPA process that enabled separate capture of electrons and holes through an ingenious interfacial reaction process between  $\text{Fe}_2(\text{MoO}_4)_3$ , PS and pollutants. As a result,  $\text{Fe}_2(\text{MoO}_4)_3$  exhibited exceptionally high activity for refractory pollutant degradation through a dual-pathway conversion process in the HPPA process, accompanied by the generation of active free radicals. The reaction rate for pollutant removal in this system was ~98 and ~59 times higher, respectively, for Fenton-like and photocatalytic oxidation alone. The photoelectrochemical performance of the  $\text{Fe}_2(\text{MoO}_4)_3$  HPPA process was also significantly enhanced by synergistic effects. A novel interfacial reaction mechanism for inhibiting electron-hole recombination was revealed. During the HPPA reaction, PS was mainly responsible for capturing the photogenerated electrons to produce  $\text{SO}_4^{\cdot-}$  ( $\cdot\text{OH}$ ). Induced by PS, the electron-rich pollutants were mainly responsible for capturing the holes and were thus oxidized and degraded. This work provides a novel strategy for inhibiting electron-hole recombination and gives a new perspective for the efficient utilization and degradation of refractory pollutants through the HPPA synergistic process between catalyst, PS and visible light irradiation.

#### Declarations of interest

None.

#### Acknowledgments

This work was financially supported by the National Natural Science Foundation of China (51838005, 51808140, 51538013, 51808142, 51808143, 51638011, 51678408), the Natural Science Foundation of Guangdong Province (2018A030313487), the National Key Research and Development Plan of China (2016YFA0203200, 2016YFC0400503), the Young Innovative Talent Project in Higher Education of Guangdong Province (2017KQNCX150), the Climbing Plan of Guangdong Province (PDJHA0393), the College Students' Innovative Entrepreneurial Training Plan Program (CX2018187) and the Science and Technology Plans of Tianjin (No. 17PTSYJC00050).

#### Appendix A. Supplementary data

Supplementary material related to this article can be found, in the online version, at doi:<https://doi.org/10.1016/j.apcatb.2019.117904>.

#### References

- [1] R.P. Schwarzenbach, B.I. Escher, K. Fenner, T.B. Hofstetter, C.A. Johnson, U. von Gunten, B. Wehrli, *Science* 313 (2006) 1072–1077.
- [2] L. Yang, L. Xu, X. Bai, P.K. Jin, *J. Hazard. Mater.* 365 (2019) 107–117.
- [3] J. Wang, S. Wang, *J. Environ. Manage.* 182 (2016) 620–640.
- [4] O.M. Rodriguez-Narvaez, J.M. Peralta-Hernandez, A. Goonetilleke, E.R. Bandala, *Chem. Eng. J.* 323 (2017) 361–380.
- [5] F. Ding, D. Yang, Z. Tong, Y. Nan, Y. Wang, X. Zou, Z. Jiang, *Environ. Sci. Nano* 4 (2017) 1455–1469.
- [6] J. He, D.W. Shao, L.C. Zheng, L.J. Zheng, D.Q. Feng, J.P. Xu, X.H. Zhang, W.C. Wang, W.H. Wang, F. Lu, H. Dong, Y.H. Cheng, H. Liu, R.K. Zheng, *Appl. Catal. B: Environ.* 203 (2017) 917–926.
- [7] T. Sakthivel, G. Venugopal, A. Durairaj, S. Vasanthkumar, X. Huang, *J. Ind. Eng. Chem.* 72 (2019) 18–30.
- [8] R. Singh, M. Kumar, H. Khajuria, S. Sharma, H.N. Sheikh, *Solid State Sci.* 76 (2018) 38–47.
- [9] J. Yu, Q. Nong, X. Jiang, X. Liu, Y. Wu, Y. He, *Sol. Energy* 139 (2016) 355–364.
- [10] L. Zhang, X.-F. Cao, Y.-L. Ma, X.-T. Chen, Z.-L. Xue, *New J. Chem.* 34 (2010) 2027.
- [11] M.N. Chong, B. Jin, C.W. Chow, C. Saint, *Water Res.* 44 (2010) 2997–3027.
- [12] S. Yan, Y. Shi, Y. Tao, H. Zhang, *Chem. Eng. J.* 359 (2019) 933–943.
- [13] F. Chen, C. Wu, J. Wang, C.P. François-Xavier, T. Wintgens, *Appl. Catal. B: Environ.* 250 (2019) 31–41.
- [14] C. Young, T.M. Lim, K. Chiang, J. Scott, R. Amal, *Appl. Catal. B: Environ.* 78 (2008) 1–10.
- [15] M.-Y. Xing, B.-X. Yang, H. Yu, B.-Z. Tian, S. Bagwasi, J.-L. Zhang, X.-Q. Gong, *J. Phys. Chem. Lett.* 4 (2013) 3910–3917.
- [16] C. Yu, J.C. Yu, *Catal. Lett.* 129 (2009) 462–470.
- [17] R. Asahi, T. Morikawa, H. Irie, T. Ohwaki, *Chem. Rev.* 114 (2014) 9824–9852.
- [18] K. Li, B. Chai, T. Peng, J. Mao, L. Zan, *ACS Catal.* 3 (2013) 170–177.
- [19] C. Yu, L. Wei, W. Zhou, J. Chen, Q. Fan, H. Liu, *Appl. Surf. Sci.* 319 (2014) 312–318.
- [20] N. Shao, J. Wang, D. Wang, P. Corvini, *Appl. Catal. B: Environ.* 203 (2017) 964–978.
- [21] N. Shao, Z. Hou, H. Zhu, J. Wang, C.P. François-Xavier, *Appl. Catal. B: Environ.* 232 (2018) 574–586.
- [22] X.D. Yu, X.C. Lin, W. Feng, *Appl. Surf. Sci.* 465 (2019) 223–231.
- [23] Y.X. Pang, H.Y. Lei, *Chem. Eng. J.* 287 (2016) 585–592.
- [24] C. Cai, H. Zhang, X. Zhong, L.W. Hou, *J. Hazard. Mater.* 283 (2015) 70–79.
- [25] F. Liu, P. Yi, X. Wang, H. Gao, H. Zhang, *Sep. Purif. Technol.* 194 (2018) 181–187.
- [26] T.T. Le, M.S. Akhtar, D.M. Park, J.C. Lee, O.B. Yang, *Appl. Catal. B: Environ.* 111–112 (2012) 397–401.
- [27] J.J. Zhang, X. Zhao, Y.B. Wang, Y. Gong, D. Cao, M. Qiao, *Appl. Catal. B: Environ.* 237 (2018) 976–985.
- [28] F. Wu, H.W. Huang, T.F. Xu, W.Y. Lu, N. Li, W.X. Chen, *Appl. Catal. B: Environ.* 218 (2017) 230–239.
- [29] L.L. Dong, T.F. Xu, W.X. Chen, W.Y. Lu, *Chem. Eng. J.* 357 (2019) 198–208.
- [30] Q. Yang, H. Choi, S.R. Al-Abed, D.D. Dionysiou, *Appl. Catal. B: Environ.* 88 (2009) 462–469.
- [31] Y.H. Guan, J. Ma, Y.M. Ren, Y.L. Liu, J.Y. Xiao, L.Q. Lin, C. Zhang, *Water Res.* 47 (2013) 5431–5438.
- [32] Y.P. Wang, C. Liu, Y.T. Zhang, W.D. Meng, B. Yu, S.Y. Pu, D.H. Yuan, F. Qi, B.B. Xu, W. Chu, *Appl. Catal. B: Environ.* 235 (2018) 264–273.
- [33] S.X. Liang, Z. Jia, W.C. Zhang, X.F. Li, W.M. Wang, H.C. Lin, L.C. Zhang, *Appl. Catal. B: Environ.* 221 (2018) 108–118.
- [34] J. Li, Y. Ren, F.Z. Ji, B. Lai, *Chem. Eng. J.* 324 (2017) 63–73.
- [35] L. Zhou, M. Sleiman, C. Ferronato, J.M. Chovelon, P. de Sainte-Claire, C. Richard, *Water Res.* 123 (2017) 715–723.
- [36] L. Zhou, C. Ferronato, J.M. Chovelon, M. Sleiman, C. Richard, *Chem. Eng. J.* 311 (2017) 28–36.
- [37] Y. Feng, D.L. Wu, Y. Deng, T. Zhang, K.M. Shih, *Environ. Sci. Technol.* 50 (2016) 3119–3127.
- [38] Y. Wang, H. Zhao, M. Li, J. Fan, G. Zhao, *Appl. Catal. B: Environ.* 147 (2014) 534–545.
- [39] Z. Wan, J. Wang, *RSC Adv.* 6 (2016) 103523–103531.
- [40] S. Patnaik, G. Swain, K.M. Parida, *Nanoscale* 10 (2018) 5950–5964.
- [41] T. Prasomsri, T. Nimmanwudipong, Y. Román-Leshkov, *Energy Environ. Sci.* 6 (2013) 1732.
- [42] R. Liang, F. Jing, L. Shen, N. Qin, L. Wu, *J. Hazard. Mater.* 287 (2015) 364–372.
- [43] M. Tamura, K. Shimizu, A. Satsuma, *Appl. Catal. A* 433 (2012) 135.
- [44] C. Brookes, P.P. Wells, G. Cibin, N. Dimitratos, W. Jones, D.J. Morgan, M. Bowker, *ACS Catal.* 4 (2013) 243–250.
- [45] S. Dai, Y. Cheng, B. Quan, X. Liang, W. Liu, Z. Yang, G. Ji, Y. Du, *Nanoscale* 10 (2018) 6945–6953.
- [46] K. Routray, W. Zhou, C.J. Kiely, W. Grünert, I.E. Wachs, *J. Catal.* 275 (2010) 84–98.
- [47] C.H. Hendon, D. Tiana, M. Fontecave, C. Sanchez, L. D'Arras, C. Sasse, L. Rozes, C. Mellot-Draznieks, A. Walsh, *J. Am. Chem. Soc.* 135 (2013) 10942–10945.
- [48] Z. Luo, R. Miao, T.D. Huan, I.M. Mosa, A.S. Poyraz, W. Zhong, J.E. Cloud, D.A. Kriz, S. Thanneeru, J. He, Y. Zhang, R. Ramprasad, S.L. Suib, *Adv. Energy Mater.* 6 (2016) 1600528.
- [49] X.J. Yang, P.F. Tian, C.X. Zhang, Y.Q. Deng, J. Xu, J.L. Gong, Y.F. Han, *Appl. Catal. B: Environ.* 134 (2013) 145–152.